

# The WFPC2 UV Survey: the BSS population in NGC 5824 <sup>1</sup>

N. Sanna<sup>1,2</sup>, E. Dalessandro<sup>2</sup>, F.R. Ferraro<sup>2</sup>, B. Lanzoni<sup>2</sup>, P. Miocchi<sup>2</sup>, R. W. O'Connell<sup>3</sup>

<sup>1</sup> *INAF-Osservatorio Astrofisico di Arcetri, largo Fermi 5, 50127 Firenze, Italy*  
*E – mail : sanna@arcetri.astro.it*

<sup>2</sup> *Dipartimento di Fisica e Astronomia, Università degli Studi di Bologna, via Ranzani 1,*  
*I-40127 Bologna, Italy*

<sup>3</sup> *Department of Astronomy, University of Virginia, P. O. Box 400325, Charlottesville, VA*  
*22904, USA*

## ABSTRACT

We have used a combination of high-resolution *Hubble Space Telescope* WFPC2 and wide-field ground-based observations, in ultraviolet and optical bands, to study the blue straggler star population of the massive outer-halo globular cluster NGC 5824, over its entire radial extent. We have computed the center of the cluster and constructed the radial density profile, from detailed star counts. The profile is well reproduced by a Wilson model with a small core ( $r_c \simeq 4.4''$ ) and a concentration parameter  $c \simeq 2.74$ . We also present the first age determination for this cluster. From the comparison with isochrones, we have found  $t = 13 \pm 0.5$  Gyr. We discuss this result in the context of the observed age-metallicity relation of Galactic globular clusters. A total of 60 bright blue stragglers has been identified. Their radial distribution is found to be bimodal, with a central peak, a well defined minimum at  $r \sim 20''$ , and an upturn at large radii. In the framework of the dynamical clock defined by Ferraro et al. (2012), this feature suggests that NGC 5824 is a cluster of intermediate dynamical age.

*Subject headings:* Globular clusters: individual (NGC 5824); stars: evolution - binaries: general - blue stragglers

---

<sup>1</sup>Based on observations with the NASA/ESA *HST* (Prop. 11975), obtained at the Space Telescope Science Institute, which is operated by AURA, Inc., under NASA contract NAS5-26555.

## 1. INTRODUCTION

The high stellar densities typical of globular clusters (GCs) make stellar interactions very likely events. For this reason it is expected that in GCs stellar evolution is strongly affected by the environment. Indeed GCs are efficient furnaces of exotic populations, like X-ray binaries, millisecond pulsars and blue straggler stars (BSSs; Paresce et al. 1992; Bailyn 1995; Bellazzini et al. 1995; Ferraro et al. 1995, 2001; Ransom et al. 2005; Pooley & Hut 2006). BSSs constitute the largest population among these “exotica”, thus representing a crucial probe of the GC internal dynamics. In the optical color-magnitude diagram (CMD) of stellar systems BSSs appear bluer and brighter than the main sequence (MS) stars, thus mimicking a population of objects younger and more massive than the normal MS turnoff stars. Indeed, direct measurements (Shara et al. 1997, Gilliland et al. 1998, De Marco et al. 2004) have shown that BSSs are two to three times more massive than the average stars in GCs ( $\langle m \rangle \sim 0.5M_{\odot}$ ).

Two main scenarios have been proposed to explain the formation of BSSs: mass transfer in binary systems (McCrea 1964; Zinn & Searle 1976) and stellar collisions (Hills & Day 1976). The two formation channels are believed to co-exist within the same cluster (see for example the case of M30 Ferraro et al. 2009; Li et al. 2013; Dalessandro et al. 2013) with efficiencies that may vary as a function of the environment (Bailyn 1992, Ferraro et al 1995). Collisional BSSs more likely form in the core or in very dense GCs because the densities are higher and so are the probabilities of direct collisions (e. g. Mapelli et al. 2004). Mass transfer is expected to be the dominant formation channel in the cluster’s outskirts or in loose environments (but see Knigge et al. 2009). Chemical signatures of the different BSS formation mechanisms have been found in 47 Tucanae (Ferraro et al. 2006a) and in M30 (Lovisi et al. 2013) where a fraction of stars shows anomalies in carbon and oxygen abundances, which are expected to be signatures of the mass-transfer process (Sarna & de Greve 1996).

Because of their mass and the mechanisms involved in their formation, BSSs are powerful tracers of the evolution of internal dynamics of clusters. In particular, as recently shown by Ferraro et al. (2012, F12), their radial distribution provides us with a measure of the dynamical friction efficiency. In fact, based on the observed shape of several BSS distributions, F12 grouped GCs in three main families. Family I is composed of clusters where the radial BSS distribution is indistinguishable from that of the reference stars, suggesting that these clusters have not undergone mass-segregation yet ( $\omega$  Centauri, Ferraro et al. 2006b; NGC 2419, Dalessandro et al. 2008a; Palomar 14, Beccari et al. 2011). Most of the clusters show a bimodal BSS radial distribution: a peak in the center, a clear dip at intermediate radii, and an upturn in the external regions. These clusters are members of Family II. Family III

is composed by clusters with a monotonically decreasing BSS distribution (M79, Lanzoni et al. 2007a; M75, Contreras Ramos et al. 2012; M80 and M30, F12). In these clusters even the most distant BSSs already drifted toward the cluster’s center. Different families correspond to different dynamical age of the clusters. As proposed by F12, Family I systems are dynamically young, Family II clusters have intermediate dynamical ages and the Family III ones are the oldest.

Being more massive than the average cluster stars, BSSs are typically found in the innermost regions of GCs, where stellar crowding and the dominant luminosity contribution of red giant branch (RGB) stars make the construction of complete samples of BSSs quite difficult in optical bands. Conversely, it is fairly easy in the UV bands (Paresce et al. 1991). In particular, high-resolution UV observations with the *Hubble Space Telescope* (HST) open the possibility to survey UV bright populations, including horizontal branch (HB; Ferraro et al. 1998; D’Cruz et al. 2000; Dalessandro et al. 2011; see also O’Connell et al. 1997 and Schiavon et al. 2012), BSSs (Ferraro et al. 1993; Ferraro et al. 1997) and post-asymptotic giant branch (see for example Brown et al. 2008) stars, even in the innermost regions.

In the framework of an extensive UV survey of more than 30 Galactic GCs conducted with the Wide Field Planetary Camera 2 (WFPC2) on board HST (Prop 11975, PI Ferraro), here we present a detailed multiwavelength photometric analysis of NGC 5824. This poorly studied cluster is located at  $\sim 26$  kpc from the Galactic center (Harris 1996, 2010 version) and, after NGC 2419, it is the most luminous outer-halo GC ( $M_V = -8.85$ , Harris 1996). Newberg et al. (2009) suggested that NGC 5824 might be associated to the Cetus Polar Stream and it could have once been a dwarf galaxy core (Georgiev et al. 2009). Using the  $Ca_{II}$  triplet measured for 17 RGB stars, Saviane et al. (2012) found a possible intrinsic iron spread of  $\sigma([Fe/H] = 0.12)$  dex in this cluster. Grillmair et al. (1995) found that the surface density profile follows a power law over almost the entire extent of the cluster. Lutzgendorf et al. (2013) have recently suggested the presence of a  $2000M_{\odot}$  black hole in this clusters.

The paper is organized as follows. Section 2 describes the data sets and the photometric and astrometric analysis. In Section 3 we determine the center of gravity and the radial density profile of the system. In Section 4 we present the first age determination for this cluster. In Sections 5 and 6 we discuss the BSS properties and present our conclusions. The summary of the paper is presented in Section 7.

## 2. OBSERVATIONS AND DATA ANALYSIS

As in our previous studies (e.g. Sanna et al. 2012 and references therein), we have used a combination of high resolution and wide-field data to resolve the stars in the central regions and to cover the entire radial extension of the cluster at the same time. We used the best quality HST and ground-based data available for this cluster.

The *HST data set* consists of a series of images collected with three different pointings of the WFPC2 in several bands, ranging from the UV to the optical. Pointing A includes 11 optical and UV images (Prop 11975, PI Ferraro) obtained through the filters F255W, F336W and F555W with total exposure times  $t_{\text{exp}} = 7200$  s,  $t_{\text{exp}} = 2700$  s and  $t_{\text{exp}} = 200$  s, respectively. Pointing B consists of 12 optical images obtained through the filters F336W, F439W and F555W (Prop 5902, PI Fahlman) with total exposure times  $t_{\text{exp}} = 1200$  s,  $t_{\text{exp}} = 3200$  s and  $t_{\text{exp}} = 300$  s, respectively. Pointing C includes three images obtained through the filter F439W (Prop 8095, PI Ibata) with total exposure time  $t_{\text{exp}} = 1200$  s. Pointings B and C exactly overlap each other. The fields of view (FOVs) of the three pointings are shown in Figure 1. The center of the cluster is located in the Planetary Camera (pixel scale  $\sim 0.05''$  pixel $^{-1}$ ) in all pointings (see Figure 1).

The *WFI data set* is composed of data obtained with the Wide Field Imager (WFI) at the 2.2 m ESO/MPI telescope. Two images per filter through the *B* and *V* bands with total exposure times  $t_{\text{exp}} = 3600$  s and  $t_{\text{exp}} = 500$  s, respectively, were retrieved from the ESO/STECF Science Archive. WFI consists of 8 CCDs with a pixel scale of  $\sim 0.238''$  pixel $^{-1}$ . The  $33' \times 34'$  field of view allowed a complete sampling of the cluster. The cluster center is located in chip #7 (see Figure 2).

The data reduction has been performed by using DAOPHOT IV package (Stetson 1987, 1994) for both the HST and the WFI data sets. The analysis of the HST images has been performed on the individual frames. As a first step we modeled the point spread function (PSF) by using  $\sim 15$  bright and almost isolated stars in each frame. Typically the same stars were chosen in each filter. With the obtained PSF models we performed a first PSF-fit on each single image by using ALLSTAR. As second step, we built a median image for each filter using IRAF tools<sup>2</sup>. Then for each median image we built a list of stars detected above a given background threshold. The lists thus obtained have been combined for each chip. For pointings A and B we built a master-list frame including only stars detected in at least two median images. With this criterion, and for pointing A in particular, we secured

---

<sup>2</sup>IRAF is distributed by the National Optical Astronomy Observatory, which is operated by the Association of Universities for Research in Astronomy, Inc., under cooperative agreement with the National Science Foundation.

a master-list complete for both hot (UV bright) and cold (UV faint) stars. The stars in the master-list have then been force-fitted to each single frame by using the ALLFRAME package (Stetson 1994). This procedure has been performed separately for pointing A, while it has been applied simultaneously to the images in pointings B and C. Unfortunately, because of the poor quality of the optical images of pointing A, we used only those of pointings B and C. Therefore the final high-resolution HST catalogue includes all the stars located in the pointings B and C. UV magnitudes have been assigned to the stars in common with pointing A.

All the raw WFI images were corrected for bias and flat-fields using standard IRAF tools. All the single images were reduced using the DAOPHOT IV package. To model the PSF, typically 100 bright and almost isolated stars in each frame have been selected. The PSF-fitting on each single image was performed by using ALLSTAR. Using DAOMATCH/DAOMASTER packages the photometry obtained for each single chip has been reported to a common reference frame (Stetson 2000) that we have chosen to be a  $50' \times 60'$  image obtained combining different ground-based data. Once all the chips were on the same reference frame, we built a master list composed by all the stars detected in at least two frames. These stars have then been forced to each single frame by using the ALLFRAME package. This choice allowed us to get full advantage of the dithering strategy adopted for these observations and to completely fill the gaps between different chips.

All the catalogues were put on the absolute astrometric system using more than 10000 stars in common with the *Guide Stars Catalogue* (GSC2.3). As a first step we obtained the astrometric solution for the entire WFI catalogue by using the procedure described in Ferraro et al. (2001, 2003) and the cross-correlation tool CataXcorr (Montegriffo, private communication). The HST (x, y) coordinates were first transformed to the HST World Coordinate System coordinates and then they were reported to the absolute astrometric system by using the stars in common with WFI. At the end of the procedure the estimated error in the absolute positions, both in right ascension ( $\alpha$ ) and declination ( $\delta$ ), is of about  $0.2''$ .

All the WFPC2 magnitudes ( $m_{255}$ ,  $m_{336}$ ,  $m_{439}$  and  $m_{555}$ ) were calibrated to the VEGA-MAG system by using the prescription by Holtzman et al. (1995) and the zero points from the WFPC2 data handbook.<sup>3</sup> We used the equations by Dolphin (2009) to correct for charge transfer efficiency. We converted the  $B$  and  $V$  magnitudes of the wide-field catalogue to the  $m_{439}$  and  $m_{555}$  VEGAMAG system, respectively, by means of the following color equations:  $m_{439} = B + 0.500 \times (B - V) + 8.800$ ,  $m_{555} = V - 0.037 \times (B - V) + 4.980$ , obtained by using

---

<sup>3</sup><http://documents.stsci.edu/hst/wfpc2/documents/handbooks/dhb>

the stars in common between the two catalogues.

In order to exclude extra-galactic sources from our analysis, we matched our catalogues with the NASA EXTRAGALACTIC DATABASE.<sup>4</sup> We found 35 objects in common (typically galaxies and quasars) which were excluded from the following analysis. The optical CMDs for the HST and WFI data sets are shown in Figure 3.

### 3. CENTER OF GRAVITY AND RADIAL DENSITY PROFILE

We determined the center of gravity ( $C_{\text{grav}}$ ) of NGC5824 from resolved bright stars taking advantage of the high-resolution of the WFPC2 data. We followed the iterative procedure described by Montegriffo et al. (1995), as already done in previous studies (see for example Sanna et al. 2012). We used the center reported by Harris (1996) as first guess of our iterative procedure. We averaged the positions  $\alpha$  and  $\delta$  of the stars contained within circles of three different radii (8", 10" and 12"), until convergence was reached. We were of course limited in this analysis by the size and the shape of the Planetary Camera FOV. In order to avoid any possible spurious effect due to incompleteness of the catalogue, we considered three samples with different limiting magnitudes ( $m_{555} = 19.5, 19.8, 20.0$ ). The obtained values agreed within  $\sim 0.2''$  and their average was therefore assumed as  $C_{\text{grav}}$ :  $\alpha(J2000.0) = 15^{\text{h}}3^{\text{m}}58.64^{\text{s}}$ ,  $\delta(J2000.0) = -33^{\circ}4'5.905''$ . This new determination is located  $\sim 0.32''$  South-West ( $\Delta\alpha \simeq -0.09''$ ,  $\Delta\delta \simeq -0.31''$ ) from the Harris center.

Starting from  $C_{\text{grav}}$ , we divided the entire data set in two sub-samples. From the HST data set we selected only stars with a distance  $r < 75''$  from  $C_{\text{grav}}$  (see Figure 1): this is named the *inner sample*, composed of 22242 stars. Even if the region at  $r < 75''$  is not entirely sampled by the WFPC2 FOV, we conservatively preferred not to complement it with ground-based data. Hence, from the WFI data set we considered all stars at  $r > 75''$  (see Figure 2), thus defining the *outer sample* consisting of 48828 objects.

We determined the projected density profile of NGC 5824 by measuring the star counts in concentric annuli covering the entire cluster extension, from  $C_{\text{grav}}$  to  $r \sim 1050''$ . In order to limit the strong contamination from field stars in the most external regions, only fiducial RGB and HB stars (see Figure 3) have been taken into account. Starting from this first selection and because of the high crowding affecting the very central regions ( $r \sim 1.5''$ ), we further limited our selections to stars with  $m_{555} < 20.0$ . We divided the entire FOV in 19 annuli centered on  $C_{\text{grav}}$  and each annulus was divided into two, three or four sub-

---

<sup>4</sup><http://ned.ipac.caltech.edu/>

sectors. In each sub-sector the ratio between the number of stars and the sampled area has been computed. The stellar density of each annulus is then obtained as the average of the corresponding sub-sector densities and the associated errors is computed from the squared root of their variance. Incomplete area coverage affecting some annuli has been properly taken into account in this procedure. The resulting radial density profile is shown in Figures 4 and 5. The three outermost annuli ( $r > 500''$ ) have been used to estimate the contribution of background stars.

We have tried to reproduce the observed density profile by using both King (King 1966) and Wilson (Wilson 1975) models. These are widely used to describe stellar systems like GCs that are thought to have reached a state of (quasi-)equilibrium. The projected density profile in both cases is characterized by a constant value in the innermost portion and a decreasing behavior outward, with the Wilson model showing a more extended outer region (for more details see, e.g., Miocchi et al. 2013). We find that the observed density profile cannot be reproduced by a standard mono-mass King model. Similar conclusions have been reached by Grillmair et al. (1995) using photographic photometry and star counts. Figure 4 shows the best fit obtained by using a King model: as can be seen, in the external regions ( $r > 30''$ ) the observed star density profile shows a radial decrease significantly steeper than predicted by the model. The profile is instead nicely reproduced by a single mass Wilson model with a concentration  $c \simeq 2.74$  and core radius (i.e., the radius at which the central surface density equals its central value)  $r_c \simeq 4.4''$  (see Figure 5). The nominal limiting radius (at which the model density drops to zero) is located at  $r \sim 2700''$ . These values are only marginally consistent with those ( $c = 2.87$ ,  $r_c = 3.88''$ ) quoted by McLaughlin & van der Marel (2005) for the Wilson model fit to fit the surface brightness (instead of the surface density) profile.

#### 4. METALLICITY SPREAD AND AGE DETERMINATION

As quoted in Section 1, Saviane et al. (2012) recently suggested that NGC 5824 shows a possible metallicity spread of the order of 0.1 dex. The position and the morphology of the RGB is a sensible function of the metallicity (see, e.g., Valenti et al. 2004). Thus, a metallicity spread is expected to produce a measurable dispersion in the color distribution of the RGB in the ( $m_{555}, m_{439} - m_{555}$ ) CMD and we can use our data to put constraints on the possible metallicity spread.

For a quantitative estimate, we followed the procedure described in previous papers (e.g., Ferraro et al. 1991, 1992) to determine the intrinsic width (IW) of the RGB. In order to minimize at most any possible bias that can artificially broaden the color distribution of

the RGB, we selected the most vertical portion of the RGB ( $18 < m_{555} < 20.5$ ) from all stars at  $r < 75''$  observed with the Wide Field 3 chip of the WFPC2. We then computed the distribution of the residuals in the  $(m_{439} - m_{555})$  color with respect to the adopted RGB mean ridge line (see the histogram in Figure 6). This has been compared with the distribution of the intrinsic photometric errors (corresponding to  $IW=0$ , solid line), and with such a distribution convolved with a metallicity spread of 0.1 dex (dashed line; note that according with theoretical isochrones,  $\delta(m_{439} - m_{555})/\delta[\text{Fe}/\text{H}]=0.0125$ ). Based on a  $\chi^2$ -test, the solid line turns out to better reproduce the observed distribution, meaning that the color distribution of the selected RGB stars is consistent with no metallicity spread ( $IW=0$ ) or with a spread smaller than 0.1 dex.

The collected data set also offers the opportunity to determine for the first time the age of NGC 5824. This is of great importance in the context of the formation scenarios of our Galaxy. In fact, studies focused on the age-metallicity relation of Galactic GCs (e.g., Dotter et al. 2010, 2011) show that two different formation histories can be distinguished: a rapid chemical enrichment for the GCs in the inner regions of the Galaxy (at a galactocentric distance  $R_{GC} < 8$  kpc), and a prolonged formation for those in the outskirts. In these studies, however, there is a lack of clusters between  $\sim 20$  and  $\sim 40$  kpc from the Galactic center, both because they are few and because the available photometric data are typically not accurate enough. In this context, the case of NGC 5824, which lies at  $R_{GC} \sim 26$  kpc (Harris 1996) is quite interesting. In order to determine the age of this cluster, we have compared the optical HST CMD with isochrones from the Girardi’s database (Bressan et al. 2012). For a more accurate determination, we have excluded the first  $30''$ , where the photometric quality is lower. We have adopted a distance modulus  $(m - M)_0 = 17.53$  and a reddening  $E(B - V) = 0.14$  (Ferraro et al. 1999). The assumed metallicity is  $[\text{Fe}/\text{H}] = -1.91$  (Harris 1996). We have superimposed to the CMD four isochrones with different ages, ranging between 12.0 Gyr and 13.5 Gyr, stepped by 0.5 Gyr (see Figure 7). From this comparison we have determined  $t = 13 \pm 0.5$  Gyr (solid line). As shown in Figure 8, the derived age puts NGC 5824 in nice agreement with the age-metallicity relation discussed by Dotter et al (2010, 2011). NGC 5824 is in the metallicity regime where the two samples of Galactic GCs (at  $R_{GC} < 8$  kpc and  $R_{GC} > 8$  kpc) share the same portion of the age-metallicity relation plane.

## 5. THE BSS POPULATION

As already done in previous studies (e.g. Lanzoni et al. 2007b; Dalessandro et al. 2008b; Sanna et al. 2012, and references therein), in order to perform a meaningful study of BSSs



in terms of both specific frequency and radial distribution we need to select a population of "normal" cluster stars, like HB or RGB stars, which are expected to be distributed as the cluster light and, for this reason, represent a reference population.

### 5.1. The BSS selection

As quoted in the Introduction, UV-CMDs are the best planes to study the hottest stellar populations in GCs. For this reason we selected the BSSs in the  $(m_{255}, m_{255} - m_{336})$  CMD. In order to minimize possible contamination from the MS turnoff and sub-giant branch, we limited the sample to  $m_{255} < 21.6$  and we also applied a selection in color:  $0 < (m_{255} - m_{336}) < 1.1$ . The adopted selection box is shown in Figure 9. Within these limits, we identified 37 BSSs from the UV.

Unfortunately, the UV data do not cover the entire extension of the cluster. Hence, as done in previous papers (see Lanzoni et al. 2007b) we "translated" the UV selection box in the optical plane in the following way: we identified the position of the UV-selected BSSs in the  $(m_{555}, m_{439} - m_{555})$  HST CMD, then we defined the boundaries of the optical selection box as to include the bulk of the UV-selected BSSs. The resulting optical selection box is shown in Figure 10. From the portion of the *inner sample* not covered by pointing A we thus selected 3 stars, for a total of 40 BSSs in the *inner sample*.

The same box has been used to selected BSSs in the *outer sample*. In this case, we limited the analysis to  $r < 500''$ , the distance at which the cluster density becomes smaller than the background density (see Figure 5). Even if this value is several times smaller than the estimated limiting radius (see Section 3), we conservatively preferred to adopt this limit to minimize the impact of contamination for Galactic field stars. In the *outer sample* we then selected 23 BSSs.

### 5.2. The reference populations

As representative of the normal cluster stars we considered both the HB and the RGB populations. Since NGC 5824 has an extended HB, the UV diagram is the best plane to select these stars. Following the same procedure adopted for BSSs, we defined the HB selection box in the UV plane (Figure 9) and we then converted this selection in the optical plane. NGC 5824 hosts 26 confirmed RR Lyrae stars (Samus et al. 2009), 19 of which are located in the FOV covered by our data (five in the *inner sample* and 14 in the *outer sample*). These have been included in the HB selection (see triangles in Figures 9 and 10). Considering the

entire cluster, from  $C_{\text{grav}}$  to  $r = 500''$ , we identified 819 HB stars, 557 in the *inner sample* and 262 in the complementary *outer sample*.

To select the RGB stars we used the optical CMDs, where these objects are bright and the branch well defined. Following the RGB mean ridge line, we limited our selection to  $m_{555} < 20.5$  (see the selection boxes in Figure 3). We thus identified 2286 RGB stars, 1478 in the *inner sample* and 808 in the *outer sample*.

### 5.3. The BSS radial distribution

As evident from the CMD shown in the right panel of Figure 3, the WFI data set is strongly contaminated by field stars. For this reason we carefully estimated the expected number of field stars in each selection box. In order to statistically quantify the Galactic field contamination we used the CMD obtained for  $r > 800''$ , where field stars define two vertical sequences roughly located at  $0.5 < (m_{439} - m_{555}) < 1$  and  $1.4 < (m_{439} - m_{555}) < 1.8$  (see Figure 11). By counting the number of stars located within the boxes used for the population selections, we derived the following values for the field star densities:  $\rho_{\text{BSS}} \sim 0.0131$  stars arcmin<sup>-2</sup>,  $\rho_{\text{HB}} \sim 0.2732$  stars arcmin<sup>-2</sup>,  $\rho_{\text{RGB}} \sim 1.3023$  stars arcmin<sup>-2</sup>. Star counts after decontamination are:  $N_{\text{BSS}} = 60$ ,  $N_{\text{HB}} = 759$ ,  $N_{\text{RGB}} = 2004$ .

Following Dalessandro et al. (2013), we divided the FOV into five concentric annuli centered on  $C_{\text{grav}}$  and, for each of them, we randomly subtracted a number of stars constrained by the computed field star densities. Figure 12 shows the statistically decontaminated cumulative radial distribution for the three selected populations. As evident, BSSs are more centrally concentrated than RGB and HB stars. The Kolmogorov-Smirnov test gives a probability of  $\sim 0.08$  and  $\sim 0.18$  that the BSS distribution is extracted from the same parent distribution as the RGB and HB stars, respectively.

For a more quantitative analysis, we computed the population ratios  $N_{\text{BSS}}/N_{\text{HB}}$ ,  $N_{\text{BSS}}/N_{\text{RGB}}$  and  $N_{\text{HB}}/N_{\text{RGB}}$  in five concentric annuli centered in  $C_{\text{grav}}$ . We adopted Poissonian errors for the populations and their propagation for the population ratios. The star counts for each annulus are listed in Table 1. Note that, due to the shape of the WFPC2 FOV, the annuli  $10'' < r < 30''$  and  $30'' < r < 75''$  are not entirely covered by our data (see Figure 1). The radial distributions of the population ratios are shown in Figure 13. The distribution of both  $N_{\text{BSS}}/N_{\text{HB}}$  and  $N_{\text{BSS}}/N_{\text{RGB}}$  is clearly bimodal, with a peak in the center, a minimum located at  $r_{\text{min}} \simeq 20'' = 5r_c$  and a rising branch in the outer regions. In contrast, the  $N_{\text{HB}}/N_{\text{RGB}}$  ratio (bottom panel) has a flat behavior across the entire extension of the cluster, as expected for normal populations following the distribution of the light.

We computed also the double normalized ratios for the three populations, defined as (Ferraro et al. 1993, 1997):

$$R_{\text{pop}} = \frac{N_{\text{pop}}^{\text{ann}}/N_{\text{pop}}^{\text{tot}}}{L_{\text{samp}}^{\text{ann}}/L_{\text{samp}}^{\text{tot}}}. \quad (1)$$

We adopted Poissonian errors for the populations and the luminosity and their propagation for the double normalized ratios.

The luminosity in each annulus has been obtained by integrating the best-fit Wilson profile and appropriately taking into account the effective area covered by the observations. The computed luminosity ratios are reported in Table 1. Figure 14 shows the results. As expected by the stellar evolutionary theory (Renzini & Fusi Pecci 1988), the HB and RGB stars follow the distribution of the light: the radial distribution is constant (grey rectangles) at a value close to unity. Again, the BSS distribution is found to be bimodal.

## 6. DISCUSSION

Following the scenario proposed by F12, the shape of the BSS radial distributions can be interpreted in terms of the dynamical age of stellar systems. In particular, the bimodal BSS radial distribution and the location of the minimum ( $r_{\text{min}} \simeq 5r_c$ ) found for NGC 5824 indicates that this cluster is a member of the intermediate dynamical-age systems (*Family II*, in the F12 classification). The BSS distribution is very similar to that found in M55 (see Figure 2 of F12), where the minimum is located at  $r_{\text{min}} \sim 4r_c$ . The rising trend toward the center is very steep in both these clusters and the minimum is well defined. This means that dynamical friction has already been effective in segregating BSSs toward the cluster center, but it has poorly affected the outskirts.

As shown in F12, there is a strong relation between the core relaxation time ( $t_{rc}$ , one of the classical theoretical indicator of the cluster dynamical age) and the position of the minimum of the BSS radial distribution measured in units of the cluster core radius ( $r_{\text{min}}/r_c$ ). This allowed F12 to define the *empirical dynamical clock*: the position of  $r_{\text{min}}/r_c$  can be used as a sort of clock time-hand to measure the dynamical age of clusters. In this framework, a flat BSS radial distribution, where  $r_{\text{min}}$  cannot be defined, indicates clusters with a relaxation time of the order of the age of the Universe (*Family I*), while a monotonic BSS radial distribution with only a central peak indicates dynamically old clusters, where the action of dynamical friction has operated out to the most remote regions of the cluster, segregating the entire BSS population in the center (*Family III*). Following F12, we have computed  $t_{rc}$  for NGC 5824 by using equation (10) of Djorgovsky (1993), adopting the cluster structural parameters obtained in Section 3. We adopted the reddening and distance modulus quoted

by Ferraro et al. (1999), the central luminosity density listed by Harris (1996) and the total cluster mass estimated by McLaughlin & van der Marel (2005). In Figure 15 we show the position of NGC 5824 (black solid circle) in the “dynamical clock plane” ( $t_{rc}/t_H$  as a function of  $r_{min}/r_c$ ; see Figure 4 in F12), where  $t_H = 13.7$  Gyr is the age of the Universe. Clearly, this cluster nicely follows the same relation defined by the sample analyzed in F12 (see also Dalessandro et al. 2013 and Beccari et al. 2013), further confirming that the shape of the observed BSS distribution is a good measure of GC dynamical ages. This figure also confirms that NGC 5824 is a mid dynamical-aged cluster of *Family II*, where the action of dynamical friction has already started to segregate BSSs (and binary systems of similar total mass) toward the cluster center. In this scenario, the most remote BSSs are thought to be still evolving in isolation in the outer cluster regions.

## 7. SUMMARY

In this paper we have used a combination of HST UV and optical images to sample the cluster center, and wide-field ground-based optical observations covering the entire cluster extension to derive the main structural parameters of the globular cluster NGC 5824 and to study its BSS population.

From the high-resolution data we derived the cluster center of gravity lying at  $\alpha(J2000.0) = 15^{\text{h}}3^{\text{m}}58.64^{\text{s}}$ ,  $\delta(J2000.0) = -33^{\circ}4'5.905''$ . We determined the radial density profile from star counts, finding that it is best fitted by a Wilson model with core radius  $r_c \simeq 4.4''$  and concentration  $c \simeq 2.74$ .

For the first time, the age of this cluster has been determined. Using isochrone fitting we found  $t = 13 \pm 0.5$  Gyr, in excellent agreement with what expected for a outer-halo Galactic GC.

A total of 60 BSSs (40 in the *inner sample* and 20 in the *outer sample*) has been identified. The comparison between the radial distribution of BSSs and normal cluster stars (HB and RGB), as well as of the double normalized ratios shows that the BSS distribution is bimodal: peaked in the center, with a clear-cut dip at intermediate-small radii ( $r_{min} \simeq 20'' \simeq 5r_c$ ), and with an upturn in the external regions. This suggests that NGC 5824 is an intermediate dynamical-age cluster.

## ACKNOWLEDGMENTS

This research is part of a Project COSMIC-LAB founded by The European Research Council (under contract ERC-2010-AdG-267675). Research at the University of Virginia was supported in part by NASA grant GO-11975 from the Space Telescope Science Institute to R. T. Rood and R. W. O’Connell.

## REFERENCES

- Bailyn, C. D. 1992, *ApJ*, 392, 519
- Bailyn, C. D. 1995, *ARA&A*, 33, 133
- Beccari, G., Sollima, A., Ferraro, F. R., Lanzoni, B., Bellazzini, M., De Marchi, G., Valls-Gabaud, D., Rood, R. T. 2011, *ApJ Letters*, 737, 3
- Beccari, G., Dalessandro, E., Lanzoni, B., et al. 2013, *ApJ*, 776, 60
- Bellazzini, M., Pasquali, A., Federici, L., Ferraro, F. R., & Pecci, F. F. 1995, *ApJ*, 439, 687
- Bressan, A., Marigo, P., Girardi, L., Salasnich, B., Dal Cero, C., Rubele, S., Nanni, A. 2012, *MNRARS*, 427, 127
- Brown, T. M., Smith, E., Ferguson, H. C., et al. 2008, *ApJ*, 682, 319
- Contreras Ramos, R., Ferraro, F. R., Dalessandro, E., Lanzoni, B., Rood, R. T. 2012, *ApJ*, 748, 91
- Dalessandro, E., Lanzoni, B., Ferraro, F. R., et al. 2008b, *ApJ*, 677, 1069
- Dalessandro, E., Lanzoni, B., Ferraro, F. R., Vespe, F., Bellazzini, M., & Rood, R. T. 2008a, *ApJ*, 681, 311
- Dalessandro, E., Salaris, M., Ferraro, F. R., et al. 2011, *MNRAS*, 410, 694
- Dalessandro, E., Ferraro, F. R., Lanzoni, B., et al. 2013, *ApJ*, 770, 45
- Dalessandro, E., Ferraro, F. R., Massari, D. et al. 2013, arXiv1310.2389
- D’Cruz, N. L., O’Connell, R. W., Rood, R. T., et al. 2000, *ApJ*, 530, 352
- De Marco, O., Lanz, T., Ouellette, J., A. Zurek, D., Shara, M. M. 2004, *ApJ*, 606L, 151

- Dotter, A., Sarajedini, A., Anderson, J., et al. 2010, *ApJ*, 708, 698
- Dotter, A., Sarajedini, A., Anderson, J. 2011, *ApJ*, 738, 74
- Dolphin, A. E. 2009, *PASP*, 121, 655
- Ferraro, F. R., Clementini, G., Fusi Pecci, F., & Buonanno, R. 1991, *MNRAS*, 252, 357
- Ferraro, F. R., Fusi Pecci, F., & Buonanno, R. 1992, *MNRAS*, 256, 376
- Ferraro, F. R., Fusi Pecci, F., Cacciari, C., Corsi, C. E., Buonanno, R., Fahlman, G. G., Richer, H. B. 1993, *AJ*, 106, 2324
- Ferraro, F. R., Fusi Pecci, F., Bellazzini, M. 1995, *A&A*, 294, 80
- Ferraro, F. R., Paltrinieri, B., Fusi Pecci, F., Cacciari, C., Dorman, B., Rood, R. T., Buonanno, R., Corsi, C. E., Burgarella, D., & Laget, M. 1997, *A&A*, 324, 915
- Ferraro, F. R., Paltrinieri, B., Pecci, F. F., Rood, R. T., & Dorman, B. 1998, *ApJ*, 500, 311
- Ferraro, F. R., Messineo, M., Fusi Pecci, F., et al. 1999, *AJ*, 118, 1738
- Ferraro, F. R., D’Amico, N., Possenti, A., Mignani, R. P., & Paltrinieri, B. 2001, *ApJ*, 561, 337
- Ferraro, F. R., Possenti, A., Sabbi, E., et al. 2003, *ApJ*, 595, 179
- Ferraro, F. R., Sabbi, E., Gratton, R. et al. 2006a, *ApJ*, 647, L53
- Ferraro, F. R., Sollima, A., Rood, R. T., Origlia, L., Pancino, E., & Bellazzini, M. 2006b, *ApJ*, 638, 433
- Ferraro, F. R., Beccari, G., Dalessandro, E., et al. 2009, *Nature*, 462, 1028
- Ferraro, F. R., Lanzoni, B., Dalessandro, et al. 2012, *Nature*, 492, 393
- Georgiev, I. Y., Hilker, M., Puzia, T. H., Goudfrooij, P., Baumagrdt 2009, *MNRAS*, 396, 1075
- Gilliland, R. L., Bono, G., Edmonds, P. D., Caputo, F., Cassisi, S., Petro, L. D., Saha, A., Shara, M. M. 1998, *ApJ*, 507, 818
- Grillmair, C. J., Freeman, K. C., Irwin, M., Quinn, P. J. 1995, *AJ*, 109, 2553
- Harris, W.E. 1996, *AJ*, 112, 1487 (2010 version)

- Hills, J. G., Day, C. A. 1976, *ApL*, 17, 87
- Holtzman, J. A., Burrows, C. J., Casertano, S., Hester, J. J., Trauger, J. T., Watson, A. M., & Worthey, G. 1995, *PASP*, 107, 1065
- Hut, P., McMillan, S., Goodman, J., et al. 1992, *PASP*, 104, 981
- King, I. R. 1966, *AJ*, 71, 64
- Knigge, C., Leigh, N., Sills, A. 2009, *Nature*, 457, 288
- Lanzoni, B., Sanna, N., Ferraro, et al. 2007a *ApJ*, 663, 1040
- Lanzoni, B., Dalessandro, E., Ferraro, F. R., et al. 2007b, *ApJ*, 663, 267
- Li, C., de Grijs, R. Deng, L., Liu, X. K. 2013, *ApJ*, 770, L7
- Lovisi, L., Mucciarelli, A., Lanzoni, B., et al. 2013, *ApJ*, 772, 148
- Lützgendorf, N., Kissler-Patig, M., Gebhardt, K., et al. 2013, *A&A*, 552, A49
- Mapelli, M., Sigurdsson, S., Colpi, M., Ferraro, F. R., Possenti, A., Rood, R. T., Sills, A., Beccari, G. 2004, *ApJ Letters*, 605, 29
- McCrea, W. H. 1964, *MNRAS*, 128, 147
- McLaughlin, D. E., & van der Marel, R. P. 2005, *ApJs*, 161, 304
- Meylan, G., & Heggie, D. C. 1997, *Astron. Astrophys. Rev.*, 8, 1
- Miocchi, P., Lanzoni, B., Ferraro, F. R., et al. 2013, *ApJ*, 774, 151
- Montegriffo, P., Ferraro, F. R., Fusi Pecci, F., & Origlia, L. 1995, *MNRAS*, 276, 739
- Newberg, H. J., Yanny, B., Willett, B. A. 2009, *ApJ*, 700, 61
- O’Connell, R. W., Dorman, B., Shah, R. Y., et al. 1997, *AJ*, 114, 1982
- Paresce, F., Meylan, G., Shara, M., Baxter, D., & Greenfield, P. 1991, *Nature*, 352, 297
- Paresce, F., de Marchi, G., & Ferraro, F. R. 1992, *Nature*, 360, 46
- Pooley, D., & Hut, P. 2006, *ApJL*, 646, L143
- Ransom, S. M., Hessels, J. W. T., Stairs, I. H., et al. 2005, *Science*, 307, 892
- Renzini, A., Fusi Pecci, F. 1988, *ARA&A*, 26, 199

- Samus, N. N., Kazarovets, E. V., Pastukhova, E. N., Tsvetkova, T. M., Durlevich, O. V. 2009, *PASP*, 121, 1378
- Sanna, N., Dalessandro, E., Lanzoni, B., Ferraro, F. R., Beccari, G., Rood, R. T. 2012, *MNRAS*, 422, 1171
- Sarna, M. J., De Greve, J. -P. 1996, *QJRAS*, 37, 11
- Saviane, I., da Costa, G. S., Held, E. V., Sommariva, V., Gullieuszik, M., Barbury, B., Ortolani, S. 2012, *A&A*, 540, 27
- Schiavon, R. P., Dalessandro, E., Sohn, S. T., et al. 2012, *AJ*, 143, 121
- Shara, M. M., Saffer, R. A., & Livio, M. 1997, *ApJ*, 489, L59
- Stetson, P. B. 1987, *PASP*, 99, 191
- Stetson, P. B. 1994, *PASP*, 106, 250
- Stetson, P. B. 2000, *PASP*, 112, 925
- Valenti, E., Ferraro, F. R., & Origlia, L. 2004, *MNRAS*, 351, 1204
- Wilson, C. P. 1975, *AJ*, 80, 175
- Zinn, R., Searle, L. 1976, *ApJ*, 209, 734

---

This preprint was prepared with the AAS L<sup>A</sup>T<sub>E</sub>X macros v5.2.

$r''_i$	$r''_e$	$N_{\text{BSS}}$	$N_{\text{BSS}}^{\text{field}}$	$N_{\text{HB}}$	$N_{\text{HB}}^{\text{field}}$	$N_{\text{RGB}}$	$N_{\text{RGB}}^{\text{field}}$	$L_{\text{samp}}^{\text{ann}}/L_{\text{samp}}^{\text{tot}}$
0	10	24	0	264	0	678	0	0.35
10	30	6	0	191	0	523	1	0.24
30	75	10	0	102	1	277	3	0.15
75	250	18	1	162	14	467	65	0.21
250	500	5	2	100	45	341	213	0.05

Table 1: Internal and external radii of the five adopted annuli, number of observed BSSs, HB and RGB stars, estimated number of contaminating field stars for each populations, and fraction of sampled light.



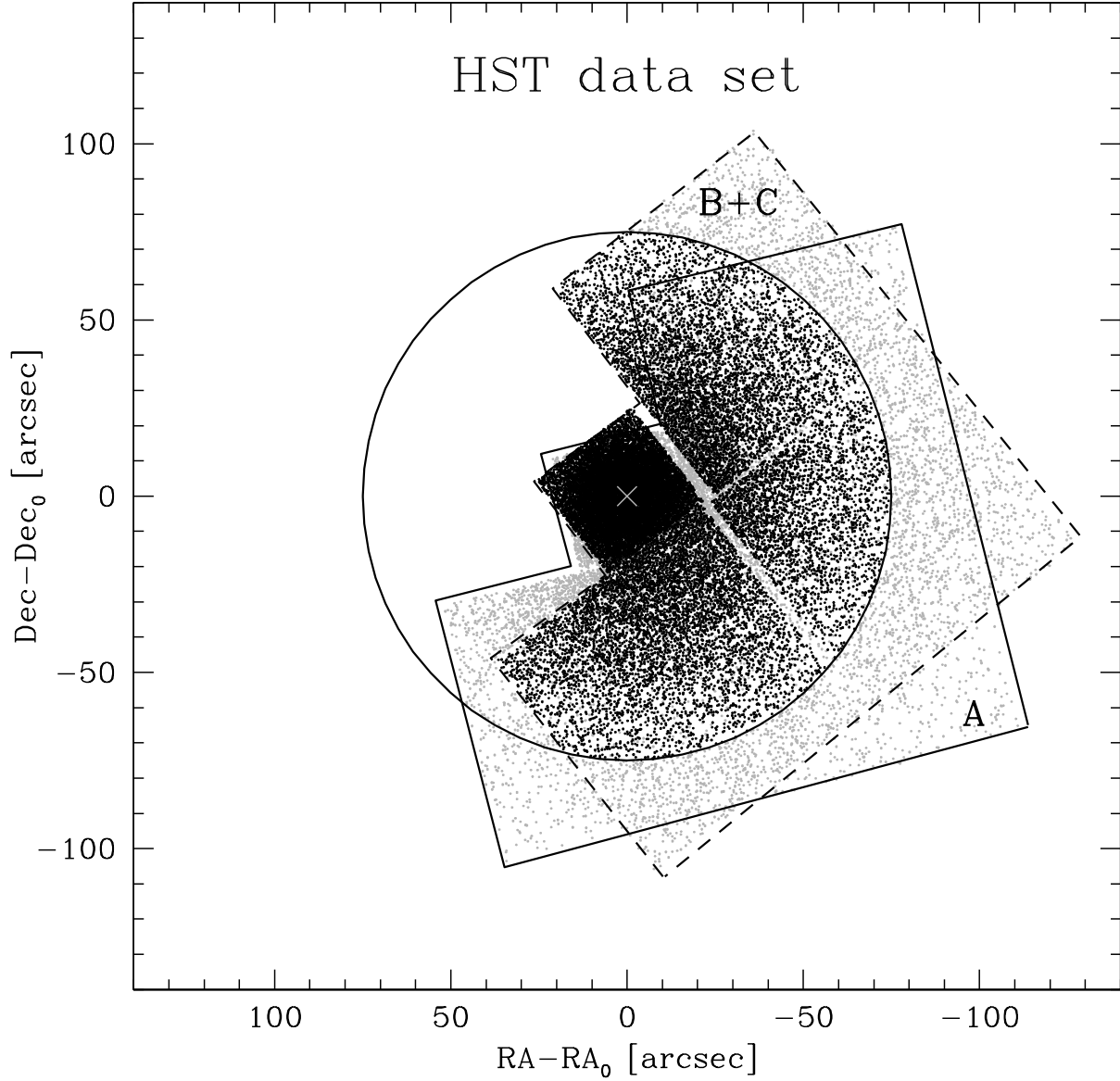


Fig. 1.— Map of the HST data set. The solid line marks the FOV of pointing A, the dashed line marks the FOV of pointings B and C, the grey cross indicates the cluster center  $C_{\text{grav}}$ . The *inner sample* (see Sect. 3) consists of all the stars (black dots) included in the FOV of pointings B+C and within a distance  $r = 75''$  from  $C_{\text{grav}}$  (solid circle).

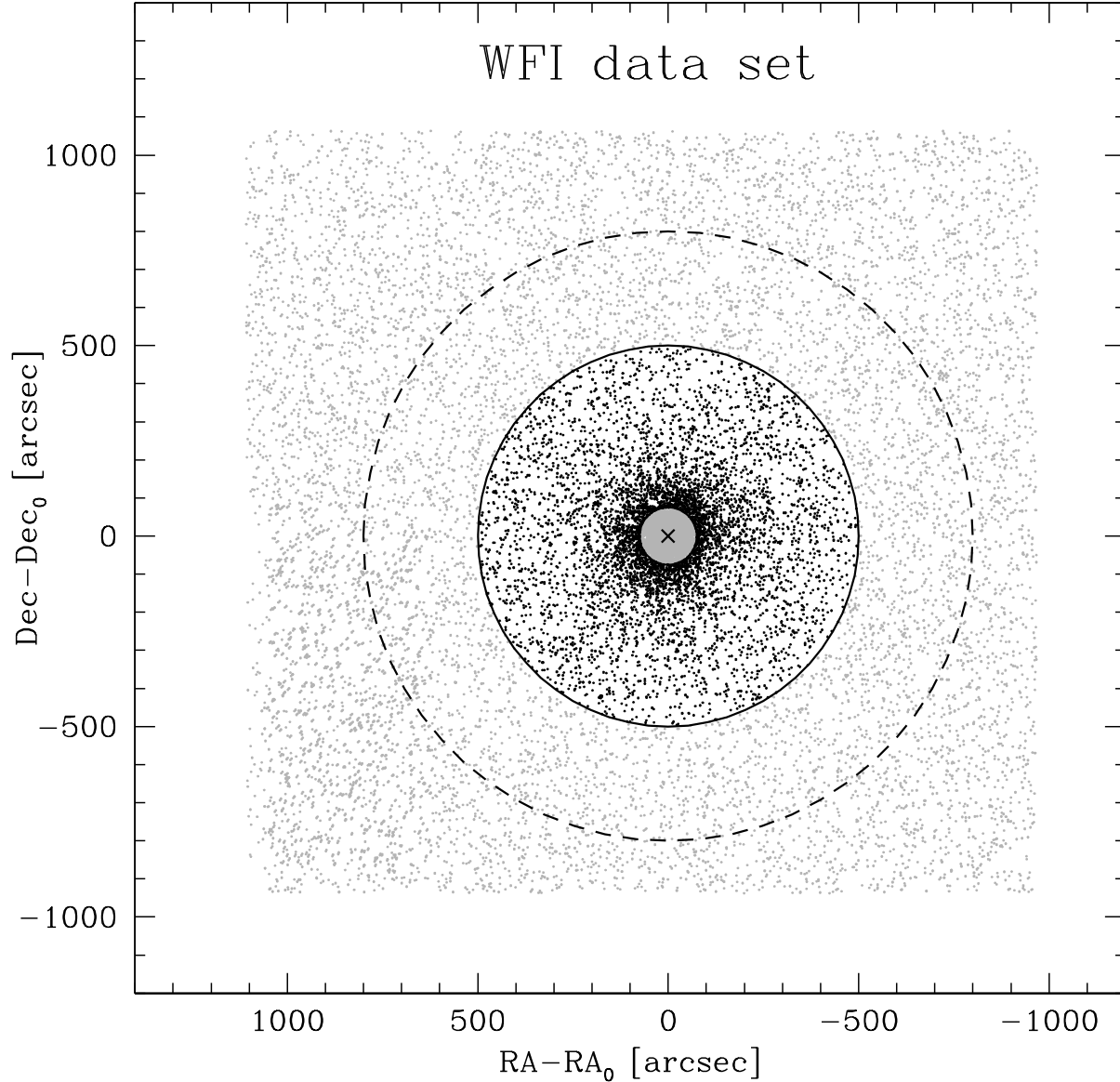


Fig. 2.— Map of the WFI data set. The *outer sample* (see Sect. 3) consists of all the stars observed at  $r > 75''$  (most internal circle). The radial distribution of the various stellar populations (BSSs, RGB and HB stars) has been studied only for  $r < 500''$  (black dots within the large solid circle), where the cluster density becomes comparable to that of field stars. To estimate the Galactic field contamination, we have used the stars observed at  $r > 800''$  (dashed circle). Only stars with  $m_{555} < 22$  are shown for the sake of clarity.

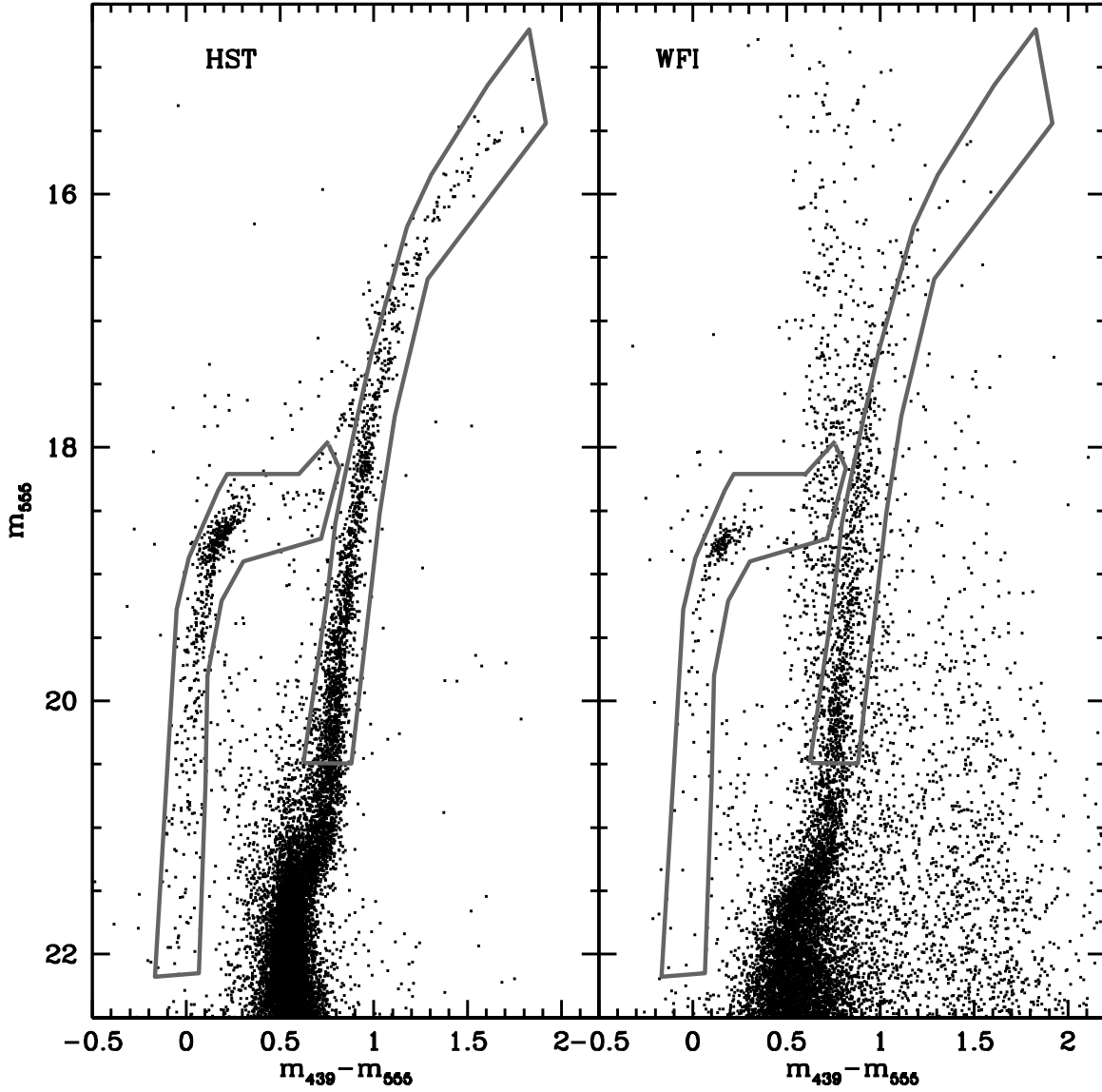


Fig. 3.— Optical CMDs of NGC 5824 for the *inner sample* (left panel) and the *outer sample* (right panel). Only the stars included in the grey boxes and with  $m_{555} < 20$  have been used to determine the density profile.

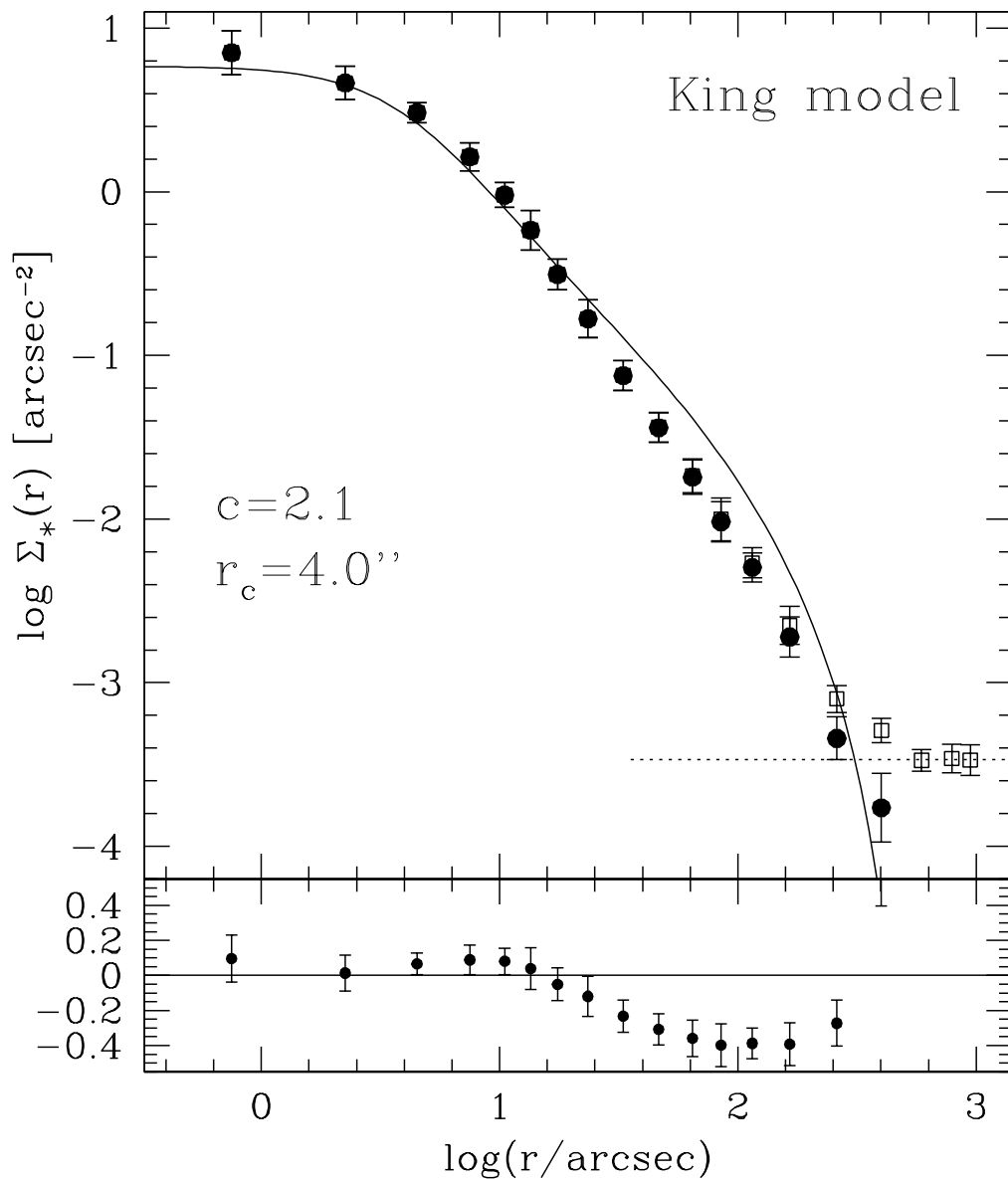


Fig. 4.— Observed surface density profile (empty squares) in units of number of stars per square arcseconds. The dotted line indicates the adopted level of the Galactic background, computed as the average of the three outermost points. Solid circles show the background-subtracted density profile. The best-fit King model is plotted as a solid line and its residuals with respect to the observations are shown in the lower panel. The labels quote the values of the model concentration and core radius.

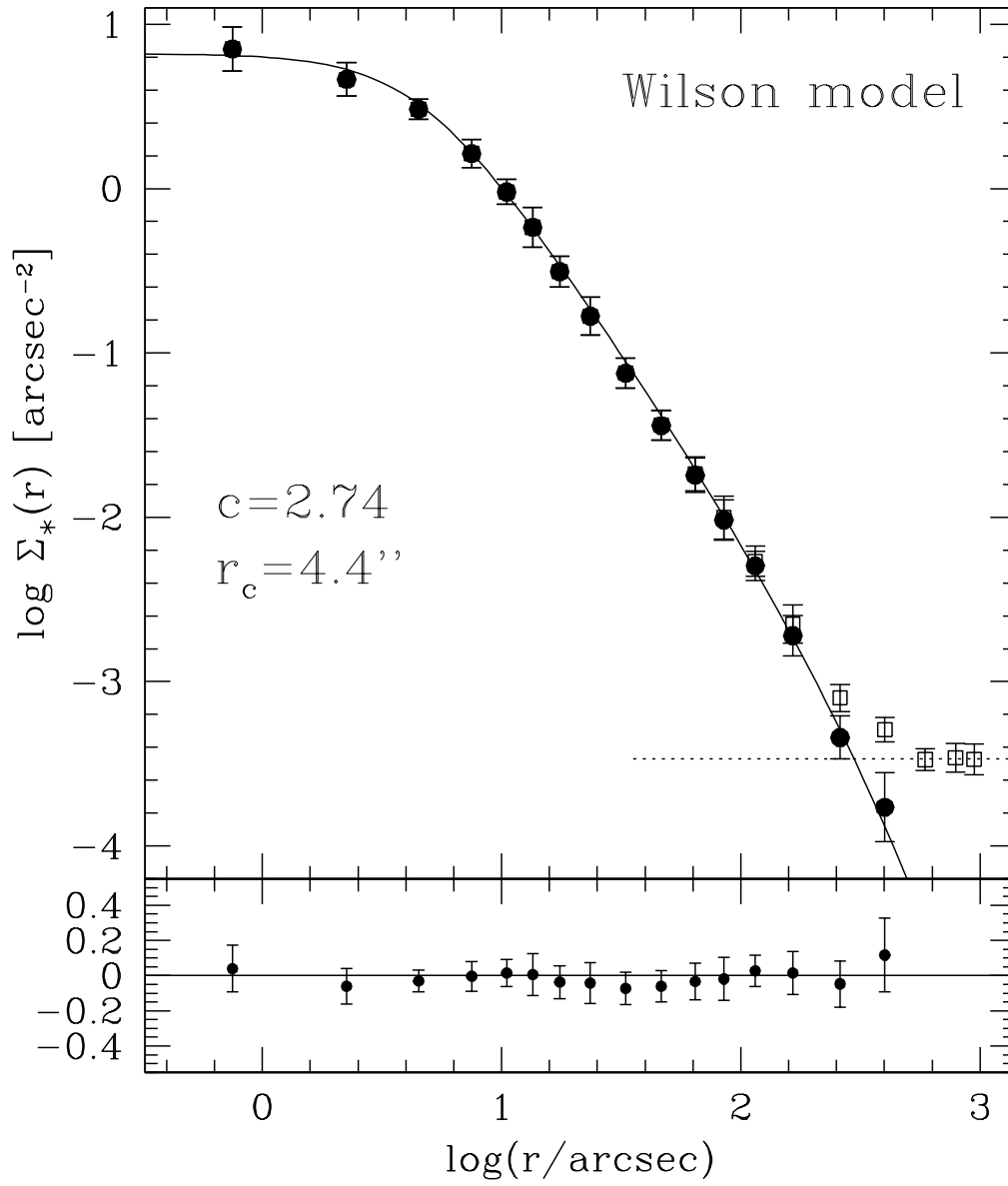


Fig. 5.— As in Figure 4, but for the best-fit Wilson model.

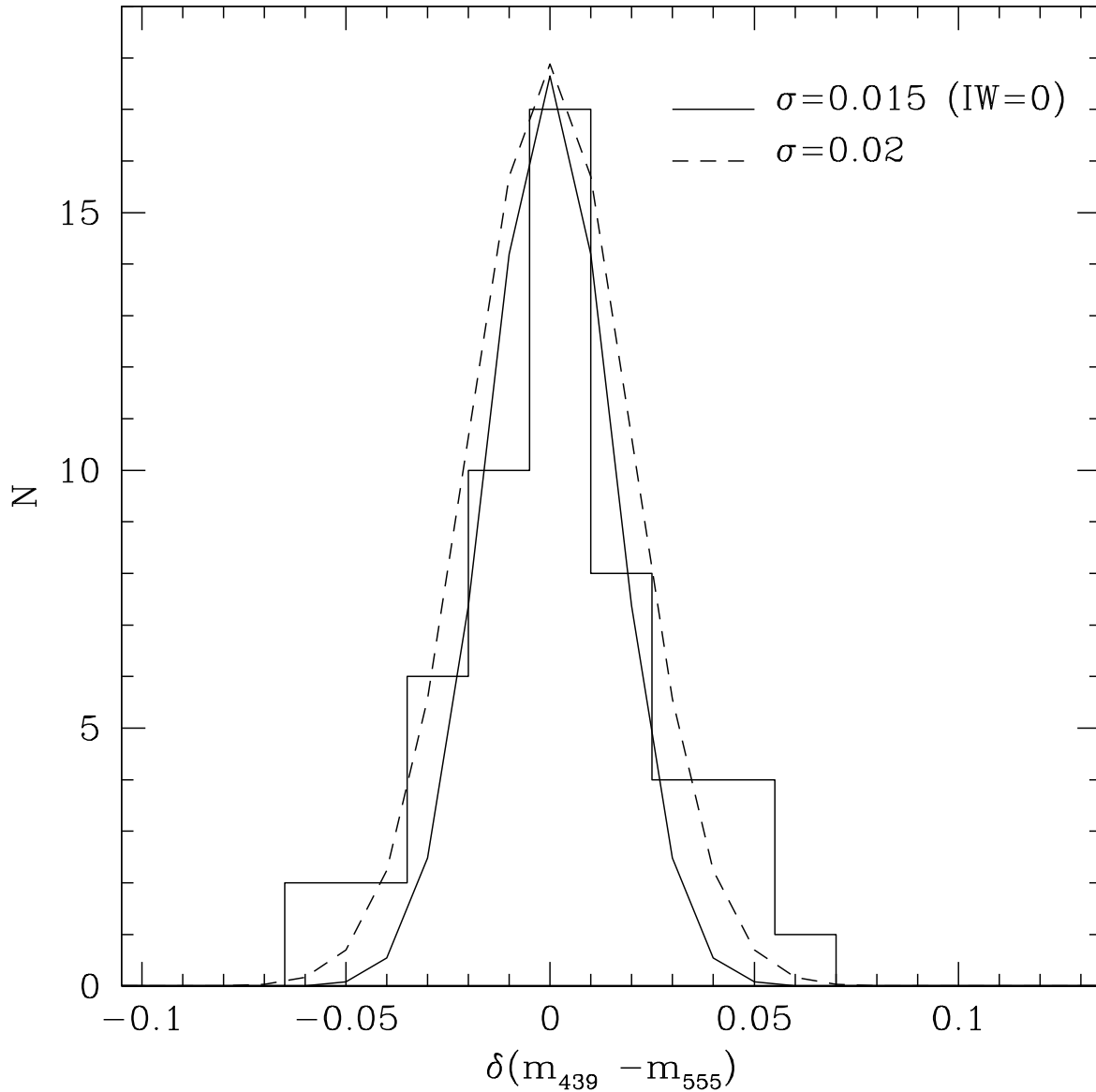


Fig. 6.— Observed color width of the RGB for the stars detected in the Wide Field 3 chip of the WFPC2, along the RGB at  $18 \leq m_{555} \leq 20.5$  and at  $r < 75''$ . The observed distribution of the  $(m_{439} - m_{555})$  color residuals with respect to the RGB mean ridge line is shown as an histogram. The solid line represents the distribution of the internal photometric errors (a Gaussian with  $\sigma = 0.015$ ), the dashed line corresponds to the same distribution convolved with a Gaussian with dispersion  $\sigma = 0.02$ , simulating a metallicity spread of  $\delta[\text{Fe}/\text{H}] = 0.1$  dex.

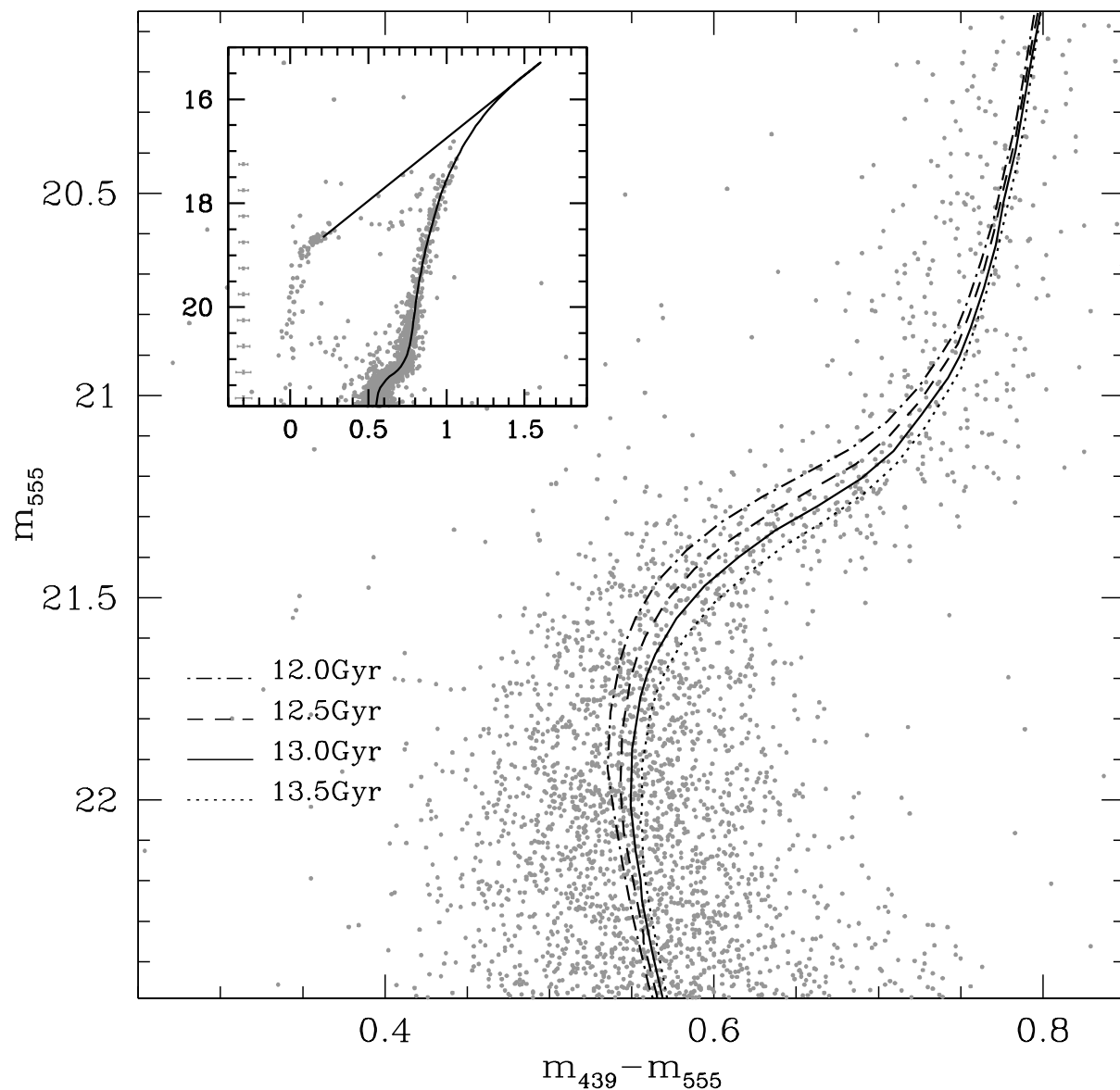


Fig. 7.— Optical CMD of the *inner sample* zoomed in the MS-turnoff region, for  $30'' \leq r \leq 75''$ . Superimposed are isochrones from the Girardi’s database computed at the cluster metallicity ( $Z = 0.000187$ ,  $[\text{Fe}/\text{H}] = -1.91$ ) and at different ages (see labels). The isochrone that best fits the observed CMD is the 13 Gyr one (solid line). The inset shows an enlarged view of the CMD.

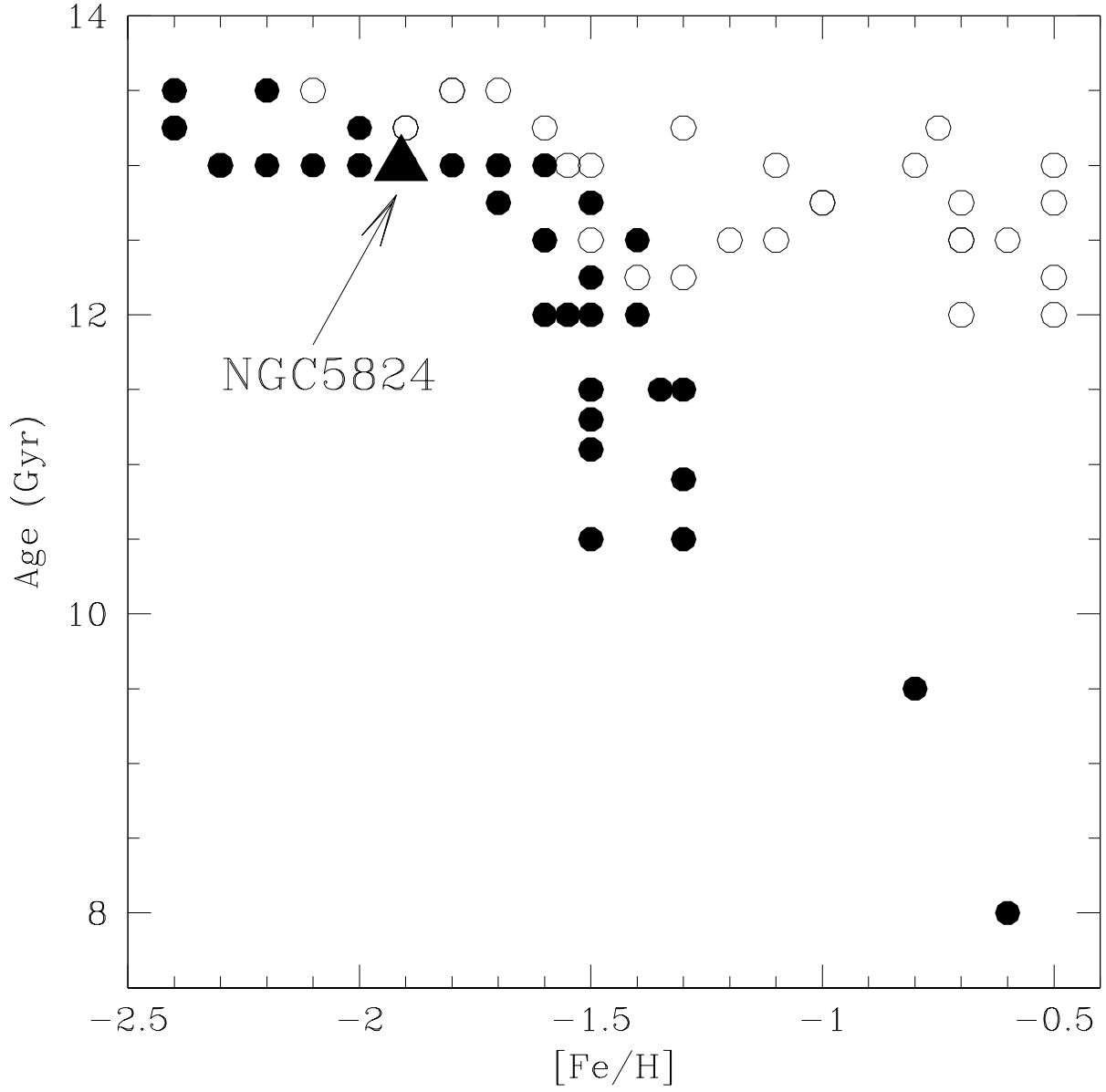


Fig. 8.— Age-metallicity relation for Galactic GCs at  $R_{GC} < 8$  kpc (open circles) and  $R_{GC} > 8$  kpc (filled circles) from Dotter et al. (2011). The position of NGC 5824 is marked by the large filled triangle.



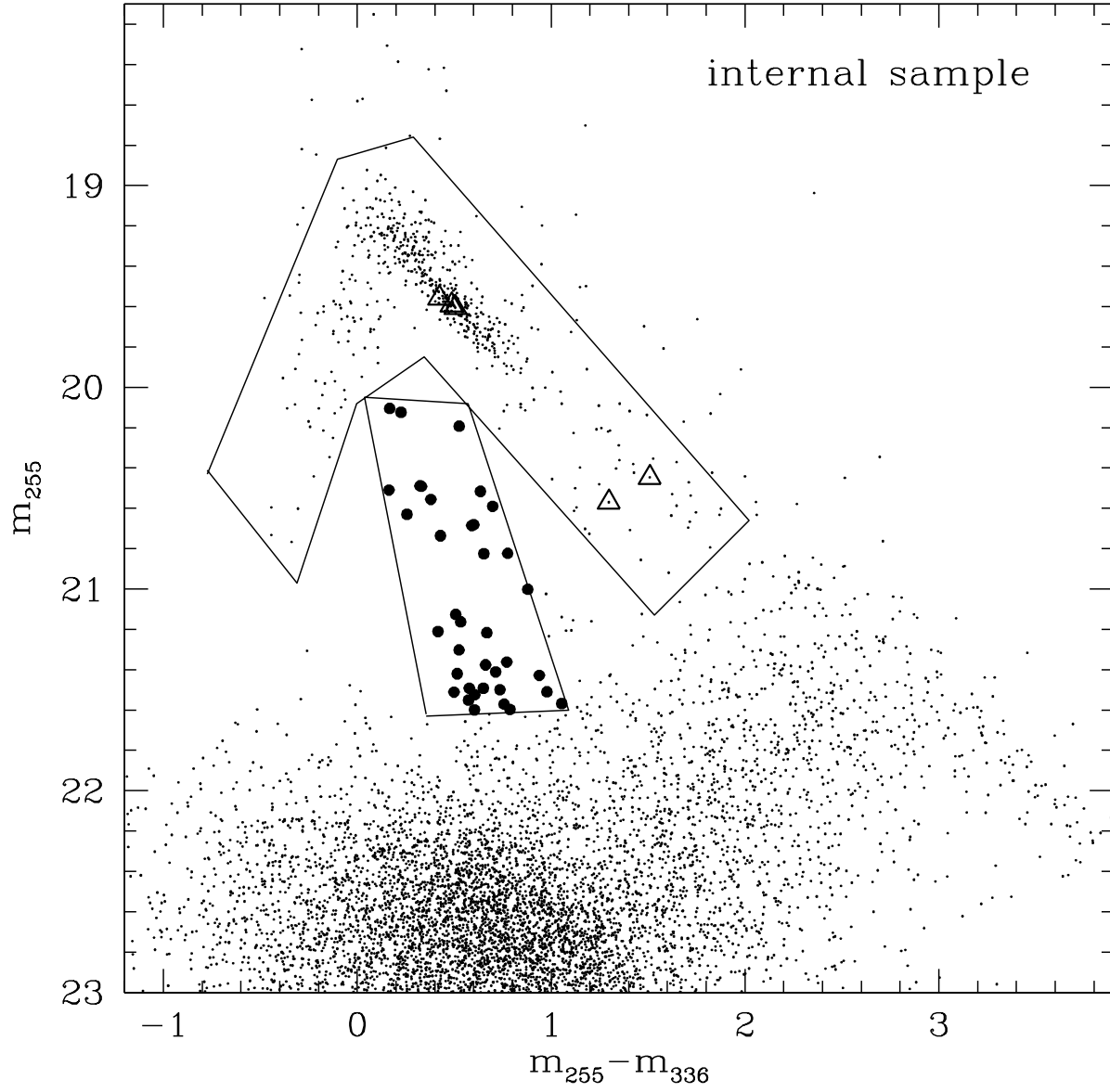


Fig. 9.— UV CMD of the *inner sample*. The adopted BSS and HB selection boxes are shown. Solid circles highlight the selected BSSs, while empty triangles mark the known RR Lyrae stars.

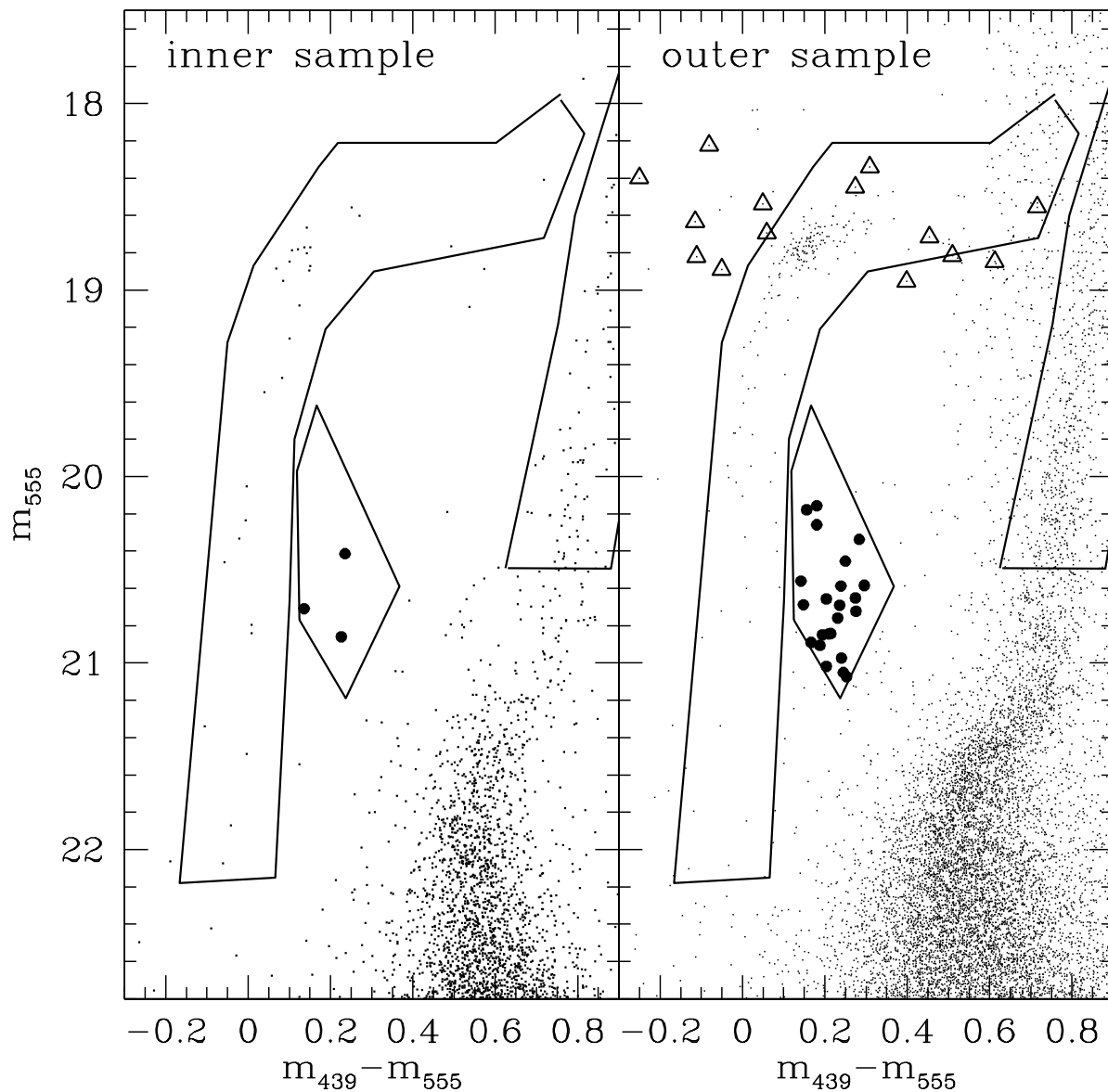


Fig. 10.— Optical CMDs of NGC 5824 zoomed in the BSS region. The left panel shows the CMD of the *inner sample* not covered by the UV data; the CMD of the *outer sample* for  $r \leq 500''$  is shown in the right-hand panel. The adopted BSS and HB selection boxes are shown with solid lines. Solid circles mark the BSSs, while empty triangles mark the known RR Lyrae stars.

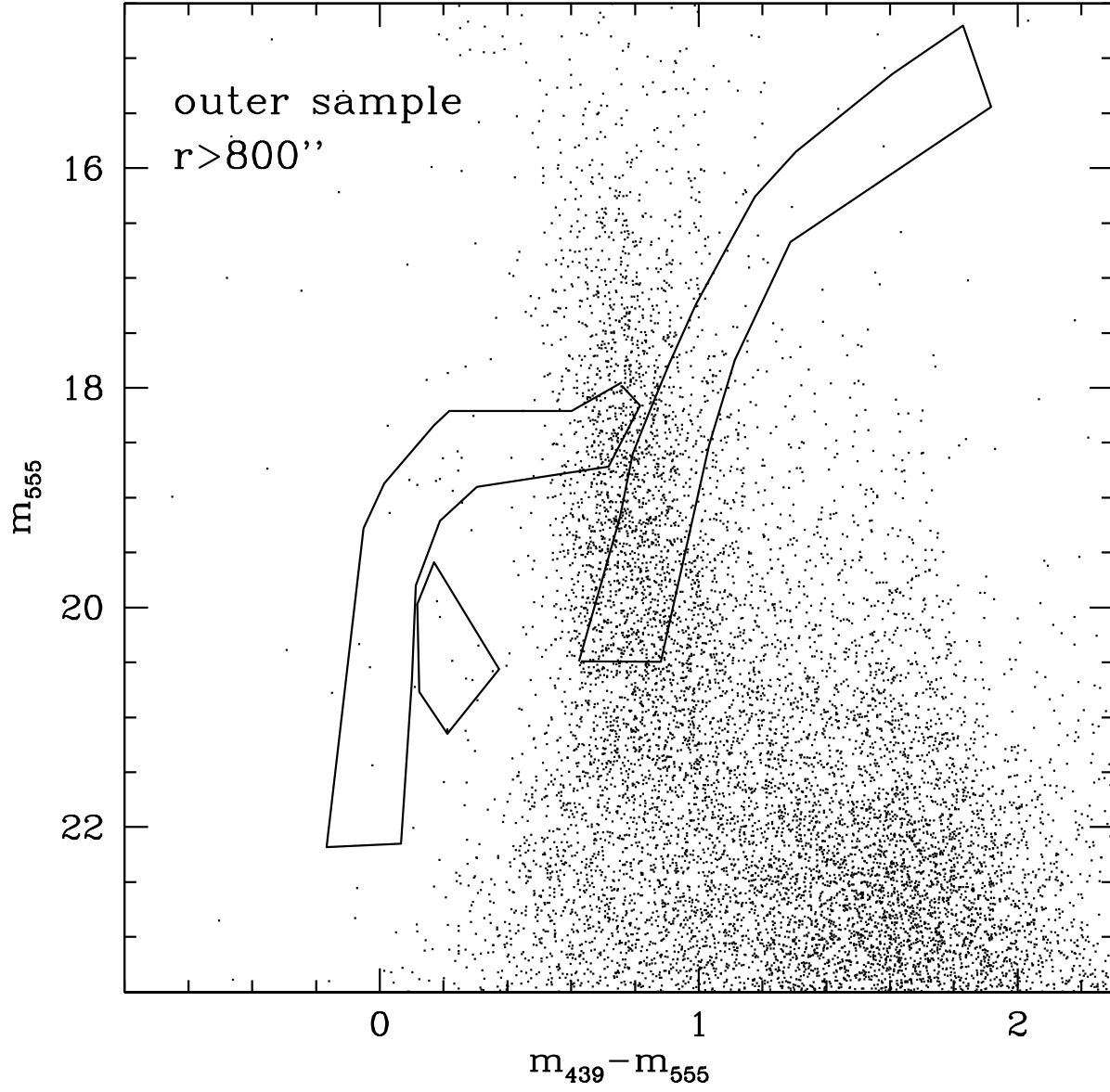


Fig. 11.— CMD of the *outer sample* at  $r > 800''$ , used to estimate the contamination of Galactic field stars to the BSS, HB and RGB population selections (the corresponding selection boxes are marked with solid lines).

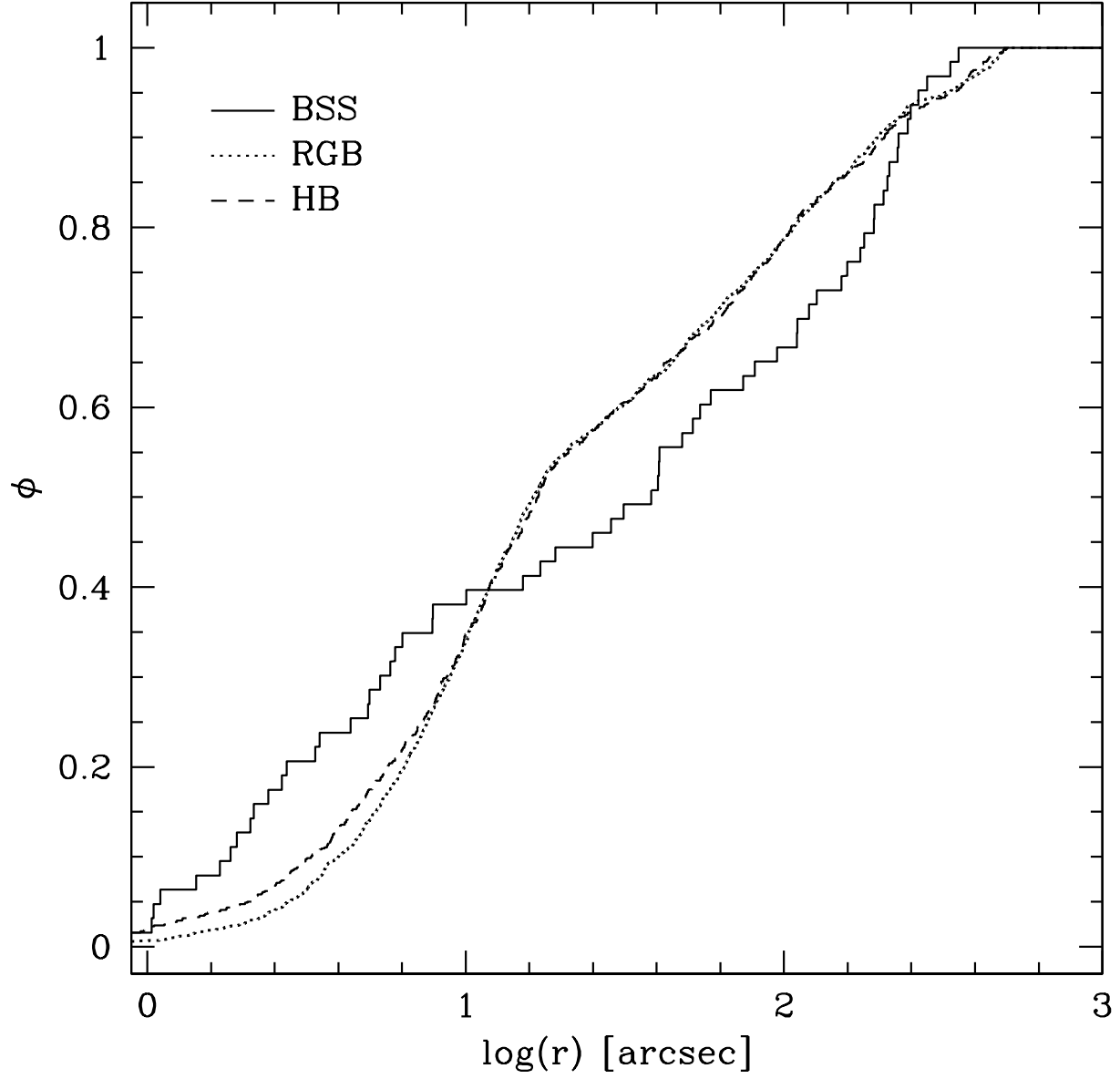


Fig. 12.— Cumulative radial distribution of the statistically decontaminated populations of BSSs (solid line), HB stars (dashed line) and RGB stars (dotted line) as a function of the projected distance from  $C_{\text{grav}}$ .

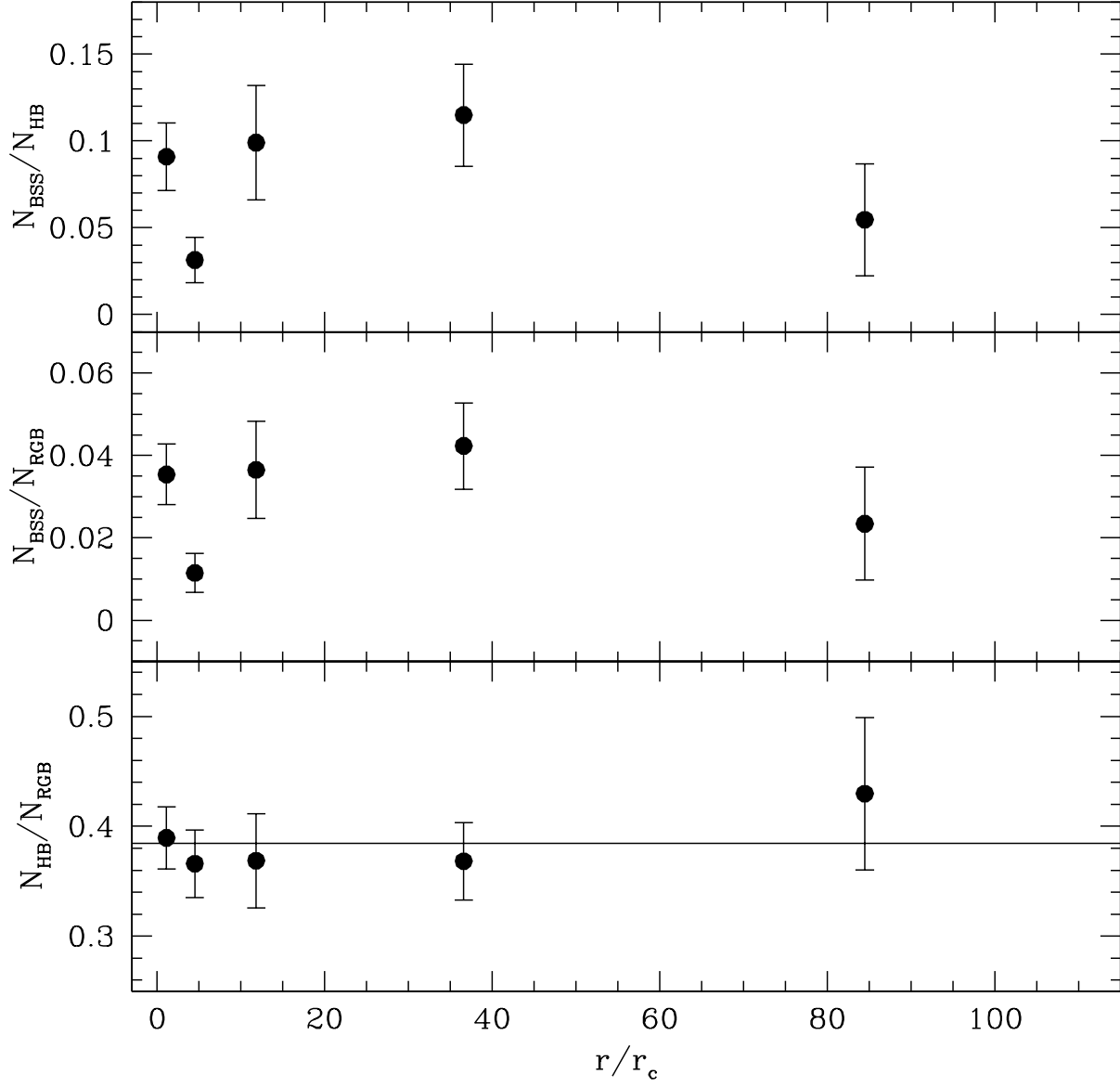


Fig. 13.— Radial distribution of the population ratios  $N_{\text{BSS}}/N_{\text{HB}}$ ,  $N_{\text{BSS}}/N_{\text{RGB}}$ ,  $N_{\text{HB}}/N_{\text{RGB}}$  (top, middle, and bottom panels, respectively) as a function of the radial distance from the cluster center, normalized to the core radius.

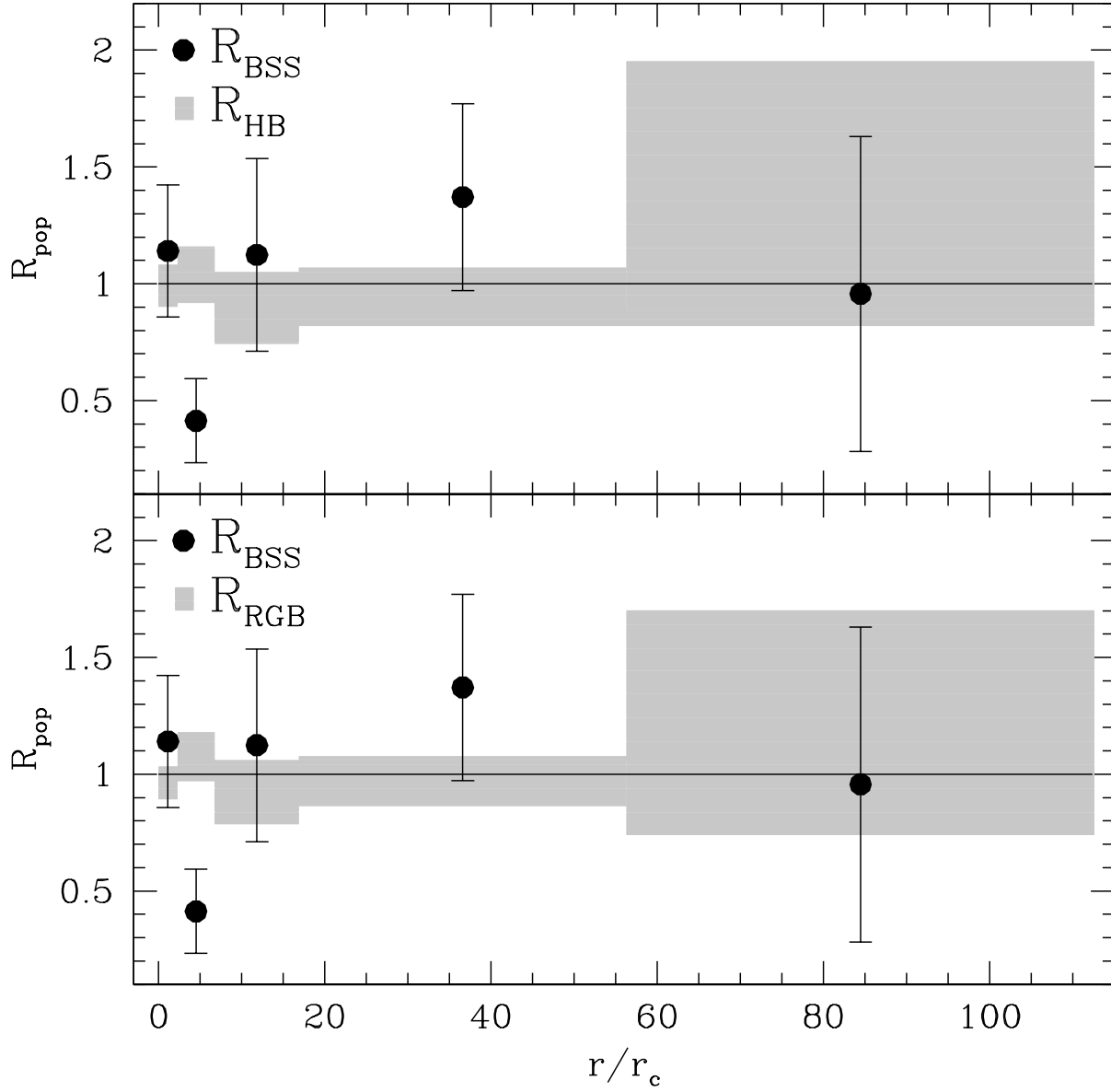


Fig. 14.— Radial distribution of the double normalized ratios of BSSs (black dots) and the references stars (grey rectangles: HB stars in the top panel, RGB stars in the bottom one).

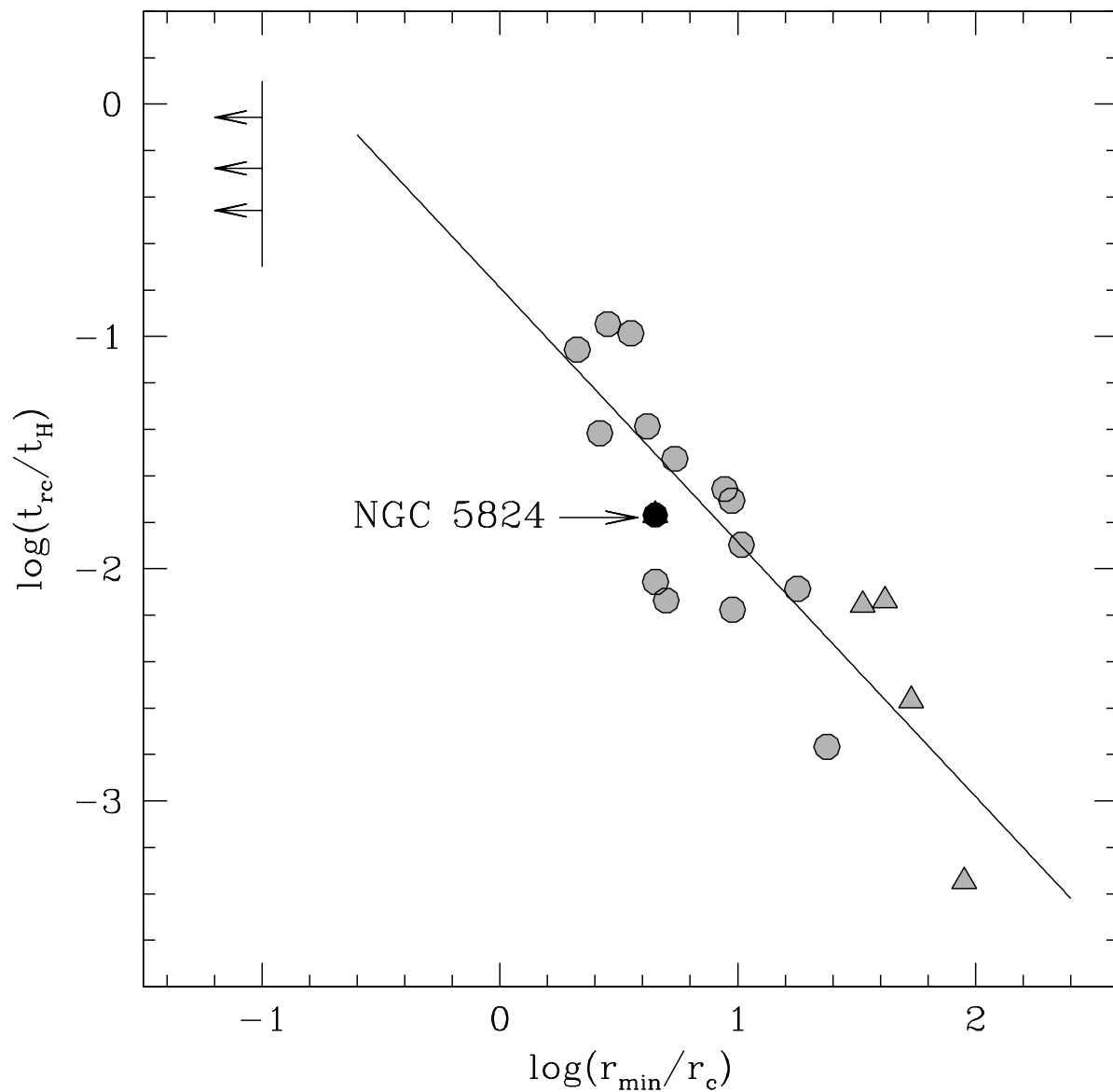


Fig. 15.— Core relaxation time ( $t_{rc}$ ) normalized to the age of the Universe ( $t_H = 13.7$  Gyr) as a function of  $r_{\min}/r_c$  (from Figure 4 of F12). The dynamically young systems (*Family I*) are plotted as lower limit arrows at  $r_{\min} = 0.1$ . The grey triangles mark the dynamically old clusters (*Family III*), while the grey circles mark the intermediate dynamical-age clusters (*Family II*). The black circle corresponds to the position of NGC 5824 in this plane.